Journal of Intelligent Manufacturing
https://doi.org/10.1007/s10845-025-02579-4

Infill pattern strategy impact on the cross-sectional area at gauge length of material extrusion 3D printed polylactic acid parts

J. M. Cañero-Nieto[1] · **R. J. Campo-Campo**[2] · **I. Díaz-Bolaño**[3] · **E. A. Ariza-Echeverri**[2] · **C. E. Deluque-Toro**[2] · **J. F. Solano-Martos**[1]

Received: 15 October 2024 / Accepted: 25 January 2025

Abstract

This study aims to explore the impact of various infill patterns on the mechanical properties of 3D-printed polylactic acid (PLA) specimens, particularly focusing on the minimum cross-sectional area, which correlates with mechanical strength. A randomized controlled trial design was employed, testing four different infill patterns: concentric, gyroid, 3D honeycomb, and rays. Each pattern was printed in PLA using a standard material extrusion 3D printer. The specimens were subjected to tensile stress using a universal testing machine, following the ASTM D638-14 standard. The cross-sectional area at gauge length was calculated using the line-plane intersection method from GCODE analysis, highlighting the minimum cross-sectional area: the weakest sections theoretically prone to failure. This work involved testing specimens with varying infill patterns to determine their influence on the mechanical integrity and performance of the parts. The concentric infill pattern exhibited the highest relative line-plane intersection points (RLPI) and maintained minimal variability in mechanical properties across the sample size. Experimental results demonstrated that different infill patterns significantly affect tensile strength, with the concentric pattern providing the most favorable outcomes in terms of strength and reliability. The choice of infill pattern in material extrusion 3D printing of PLA significantly influences the mechanical properties, particularly the tensile strength and distribution of material within the cross-sectional area. The concentric pattern consistently outperformed other types in maintaining structural integrity under stress. These findings provide crucial insights for optimizing 3D printing settings to enhance the durability and performance of printed parts.

Keywords 3D printing · Material extrusion · Polylactic acid · Infill patterns · GCODE analysis

Introduction

The advent of 3D printing technologies has fundamentally transformed materials science and engineering by enabling the creation of complex geometries with customized properties. This innovation is particularly impactful in the use of polymers such as polylactic acid (PLA), polycarbonate (PC), and acrylonitrile butadiene styrene (ABS), where precise control over 3D printing parameters can significantly alter material characteristics (Cadete et al., 2024; Exley et al., 2024; Hasan et al., 2024; Mushtaq et al., 2024; Pazhamannil et al., 2022). For instance, studies like those conducted on ABS have demonstrated that variations in layer thickness can crucially influence mechanical performance, highlighting the intricate relationship between manufacturing processes and the resulting material properties (Galina et al., 2016). Concurrently, advances in fabrication technologies such as Fused Deposition Modeling—FDM— (Schmidt & Kyosev, 2023; Zohdi et al., 2024), selective laser sintering (Song et al., 2024), and stereolithography (Tavangarian et al., 2024) have broadened the potential for producing components

---

✉ E. A. Ariza-Echeverri
earizaec@unimagdalena.edu.co

[1] Department of Civil, Materials and Manufacturing Engineering, Escuela de Ingenierías Industriales, Universidad de Málaga, Andalucía Tech, Campus de Teatinos, 29071 Málaga, Spain

[2] Grupo de Nuevos Materiales y Didáctica de Las Ciencias, Facultad de Ingeniería, Universidad del Magdalena, Santa Marta, Colombia

[3] Grupo de Investigación y Desarrollo en Sistemas y Computación, Facultad de Ingeniería, Universidad del Magdalena, Santa Marta, Colombia

with enhanced mechanical, electrical, and functional properties. These capabilities are proving transformative across high-stakes industries, including biomedical, electronics, and aerospace, where material performance can dictate the success of applications (Sandanamsamy et al., 2023a, 2023b; Song et al., 2024).

Material extrusion or FDM of PLA stands out for its eco-friendliness, biocompatibility, and extensive applications across various industries. Insights from Wang et al. (Wang et al., 2017) emphasize how varying FDM parameters can affect PLA's mechanical outcomes, advocating for strategic modifications like filler reinforcements to enhance the sustainability and performance of 3D printed parts. Investigations by Hsueh et al. (Hsueh et al., 2021) and Shanmugam et al. (Shanmugam et al., 2021) have explored how printing conditions impact PLA's tensile strength and fatigue resistance, illustrating the necessity for meticulous parameter optimization to achieve optimal material characteristics under various loading conditions. The application of metal particulate reinforcements in PLA, for example, has demonstrated promising potential to intensify the mechanical integrity of printed materials, suggesting a pathway towards more robust and efficient manufacturing solutions (Vakharia et al., 2021). Similarly, investigations into the effects of raster orientation and printing speed have revealed substantial impacts on material strength and elasticity, underlining the importance of parameter optimization for achieving superior performance (Khosravani et al., 2022). Additionally, comparative studies of PLA and ABS structures produced by FDM has emphasized the influence of fill density and other parameters on product behavior, guiding the optimization of design and production processes in FDM (Özsoy et al., 2021). The anisotropic behavior of PLA, impacted by printing orientation, illustrates how different mechanical properties such as tensile strength and elasticity can vary, providing essential insights for tailoring printing strategies to specific application needs (Morettini et al., 2022). Investigations into the variability of filling percentages and raster styles further highlight factors that significantly enhance mechanical performance, highlighting the importance of thoroughly optimizing processes to refine end-product quality (Singh et al., 2022).

Moreover, studies exploring the effects of process parameters like raster angle and printing temperature have shown their critical role in enhancing the performance of PLA, highlighting the intricate relationship between processing parameters and material characteristics (Sandanamsamy et al., 2023). Sustainable practices are also being incorporated into manufacturing, as seen in the integration of recycled materials to enhance the flexural strength of composites, thus promoting environmentally friendly production methods (Chawla et al., 2021). A systematic application of Design of Experiments (DOE) across various materials including PLA, ABS, and Nylon + CF manufactured by 3D FDM printing, significantly advancing the field by detailing the interaction between material properties, printing conditions, and mechanical performance (Rodríguez-Reyna et al., 2022). Additionally, recent insights from Kechagias and Zaoutsos (Kechagias & Zaoutsos, 2024) have outlined the crucial role of porosity in FDM parts, highlighting how printing parameters influence porosity and thus affect structural strength and durability. Their research underscores the intricacies of parameter optimization needed to balance part density and functionality, vital for maintaining material integrity under both static and dynamic loadings. Such enhancements are critical as they facilitate the creation of components with tailored mechanical properties suited for demanding industrial uses.

Recent advancements underscore the significance of infill configurations in enhancing the performance of 3D-printed components. Research by Birosz et al. (Birosz et al., 2022) and De Bernardez (De Bernardez et al., 2023) demonstrated that varying infill patterns can significantly influence the strength, flexibility, and durability of PLA structures, underscoring the need to customize these settings for specific uses. These findings are supported by Birosz and Andó (Birosz & Andó, 2024), who delve into the scalability of these patterns, suggesting that even subtle adjustments in infill geometry can profoundly affect the properties of materials. Further studies by Kadhum (Kadhum et al., 2023) demonstrate how small changes in infill density and pattern can impact not only the structural integrity but also the surface quality of printed parts. This is complemented by Dev and Srivastava (Dev & Srivastava, 2021), who have explored bio-inspired infill patterns that not only enhance mechanical properties but also promote sustainability within the manufacturing process. Together, these studies indicate a shift towards using advanced computational models to predict and optimize the outcomes of specific infill configurations, potentially revolutionizing design processes in industries such as automotive and aerospace where tailored material properties are critical. Continuing this trend, Patel et al. (Patel et al., 2023, 2024) investigate the application of these principles to the creation of carbon fiber reinforced composites, further expanding the understanding of how process parameters can be adjusted to produce materials that meet high-performance standards. This body of research underscores the potential of 3D printing to significantly improve product reliability and performance, particularly in applications where material failure is not an option, promoting for more resilient and efficient manufacturing solutions.

In addressing the gaps identified in prior studies, this research explores the interaction between various infill patterns and the mechanical integrity of 3D-printed PLA objects under different environmental conditions. While earlier works have primarily focused on the impact of single variables on mechanical properties, this study comprehensively analyzes the combined effects of infill patterns, material compositions, and environmental factors on the structural integrity and performance of printed objects. This multifaceted approach allows for a deeper understanding of the complexities involved in FDM printing, thereby providing innovative insights into optimizing 3D printing applications for enhanced durability and performance in industries such as aerospace, automotive, and biomedical engineering. Therefore, this study seeks to deepen the understanding of how infill patterns influence the mechanical properties of 3D-printed objects, addressing a notable gap in the existing research. Prior studies have extensively assessed various 3D printing parameters, yet the specific effects of infill patterns on the structural integrity and performance of printed parts remain less explored. By employing the well-established ASTM D638 − 14 standard, this research methodically analyzes the tensile properties of PLA specimens produced through FDM. Distinct infill patterns—concentric, gyroid, 3D honeycomb, and rays—were selected for their potential to enhance material strength and reliability. The thorough testing of each pattern specifically aimed to assess their impact on the distribution and strength of PLA, particularly targeting the minimum cross-sectional areas vital for assessing part integrity. The findings demonstrated how different infill choices can significantly influence the mechanical performance of PLA, providing insights for industries that depend on highly reliable and precise 3D printing technologies, such as aerospace, automotive, and biomedical engineering. These results not only underscore the necessity for strategic adjustments in 3D printing to optimize component durability and functionality but also highlight the intricate relationship between selected infill patterns and their resultant material properties. By showcasing the substantial impact of these choices, the research contributes novel perspectives to the ongoing refinement of additive manufacturing processes, ensuring that 3D printed objects meet the rigorous demands of modern engineering applications.

This study introduces a novel approach to the analysis of 3D-printed PLA components, uniquely combining experimental data with computational simulations to evaluate the influence of infill patterns on mechanical properties. Unlike previous studies which primarily focus on isolated aspects of 3D printing, this research integrates practical testing with advanced predictive models to offer a comprehensive understanding of how various infill configurations impact material behavior and performance. This dual approach is critical for developing applications where precision and reliability are paramount, such as in aerospace and biomedical engineering. Thereby, the novelty of this work lies in its methodical examination of the interaction between infill patterns and the mechanical integrity of printed structures, informed by both empirical evidence and computational insights. By doing so, the study fills a significant gap in additive manufacturing research, providing nuanced insights into the optimization of printing parameters that enhance material durability and functionality. This integrative analysis not only advances the theoretical framework of 3D printing technologies but also establishes practical guidelines for tailoring material properties to specific application needs, paving the way for future innovations in high-performance composite manufacturing. In this regard, this research is motivated by the need for a more holistic understanding of 3D printing processes, particularly in how structural variables such as infill density and pattern geometry can be optimized to improve product performance. Through a systematic exploration of these factors, combined with the robust predictive capabilities of computational modeling, this study offers new perspectives on the potential of additive manufacturing to create highly customized, functionally superior materials.

Material and methods

This study involves a detailed analysis of the mechanical properties attributed to different infill patterns in specimens printed with polylactic acid (PLA). To achieve this, a large sample of specimens representing each chosen infill pattern was produced. These specimens were subsequently tested for their mechanical properties using a universal testing machine (UTM). The assessments of these properties were primarily based on an examination of the variation in cross-sectional area along the gauge length of the specimens. This involved a meticulous analysis of the printer's trajectory during the filament deposition process, which was accomplished by processing the CNC code (GCODE) generated by the slicing software (PrusaSlicer, 2.6.0) before downloading on the printer. The resulting mechanical properties were derived from the stress–strain curves obtained during these tests. Additionally, statistical analysis was conducted on the data gathered from the population of specimens to compare and demonstrate the influence of different infill patterns on mechanical performance.

Specimen characteristics

For the experimental analysis, Type-V specimens as defined by the ASTM D638-14 standard (ASTM D638, 2014) were utilized. The material chosen for these specimens was a commercial-grade PLA filament, specifically the Ender Creality PLA + in red. This filament has a diameter of 1.75 mm with a tolerance of ± 0.05 mm and a density of 1.24 g/cm^3. Figure 1 displays the dimensional drawing of the tensile specimen alongside an image of a specimen as printed by the 3D printer. Additionally, Table 1 provides the dimensions and tolerances of the specimens in accordance with the ASTM D638-14 standard.

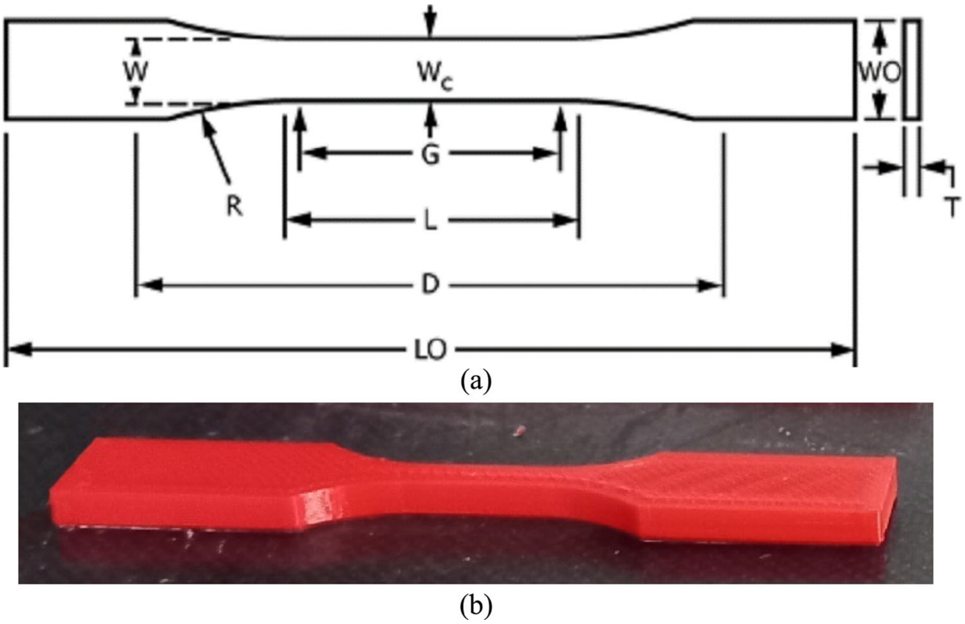

Fig. 1 **a** ASTM D638-14 dimensional drawing of tensile specimen and **b** a printed PLA specimen

Table 1 ASTM-D638 specimen dimensions

Dimension	Description	Value (mm)	Tolerance (mm)
W	Width of narrow section	3.18	± 0.5
L	Length of narrow section	9.53	± 0.5
WO	Width overall, min	9.53	± 3.18
LO	Length overall, min	63.5	no max
G	Gauge length	7.62	± 0.25
D	Distance between grips	25.4	± 5
R	Radius of fillet	12.7	± 1
T	Thickness	3.2	± 0.4

Initially, seventeen different infill patterns were examined, as illustrated in Fig. 2, with the rays pattern added subsequently. After a preliminary assessment, four patterns—concentric, gyroid, 3D honeycomb, and rays—were selected for detailed investigation. Specimens representing each of these patterns were then subjected to tensile tests to evaluate their mechanical properties.

Printer and parameter setup

The specimens were printed using a Creality Ender-3 V2 printer, equipped with a 0.4 mm extruder nozzle, as depicted in Fig. 3. The printing process was carried out at a room temperature of 25 °C and 50% relative humidity without observing, at any time, differences or anomalies in the printed

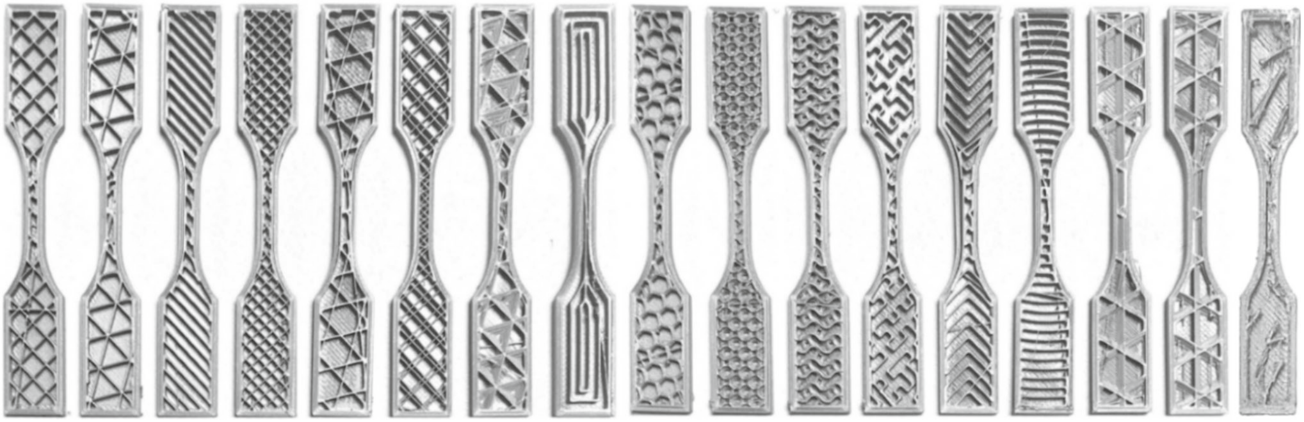

Fig. 2 From left to right, the Infill patterns are as follows: Rectilinear, Triangles, Aligned Rectilinear, Grid, Stars, Line, Cubic, Concentric, Honeycomb, 3D Honeycomb, Gyroid, Hilbert Curve, Octagram Spiral, Archimedean Chords, Adaptative Cubic, and Support Cubic

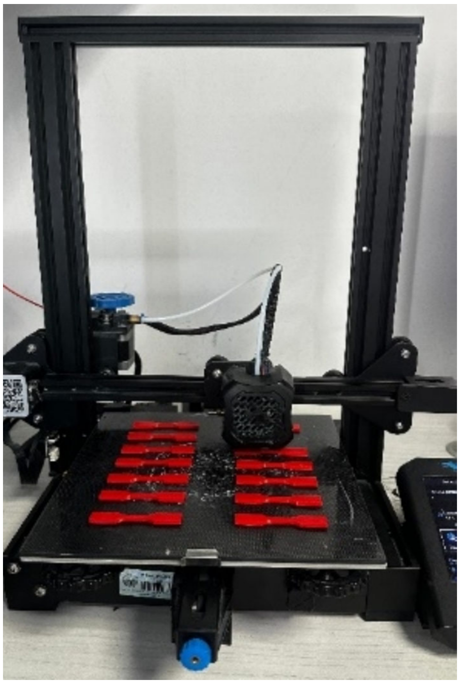

Fig. 3 Creality Ender-3 V2 printing a batch of PLA specimens

Table 2 3D printer settings

Parameter	Value	Parameter	Value
Nozzle diameter	0.4 mm	Nozzle temperature	200 °C
Extrusion width	0.4 mm	Bed temperature	60 °C
Layer height	0.2 mm	Infill density	15%
Total layers	16	Specific pattern layers	7
Solid bottom layers	3	Solid top layers	3
Bottom/top infill angle	± 45°	Bottom/top infill pattern	monotonic
Bridging layers	1	Bridging infill pattern	monotonic
Bridging infill angle (3D honey comb)	0°	Bridging infill angle (gyroid)	30°
Bridging infill angle (concentric)	65°	Bridging infill angle (rays)	75°
Perimeter	2 turns	External perimeter	1 turn
Infill speed (3D honey comb)	≈ 38 mm/s	Infill speed (gyroid)	≈ 32 mm/s
Infill speed (concentric)	43.4 mm/s	Infill speed (rays)	≈ 35 mm/s

specimens. A flat orientation was employed for building the specimens. Table 2 summarizes the configuration parameters of the 3D printer. Each specimen comprised 16 layers, which included bottom and top solid infill layers, bridge layers, and layers featuring the selected infill patterns. The fill percentage was uniformly set at 15%. Additionally, the infill speed and the raster angle for each pattern are detailed, ensuring precise replication of experimental conditions.

The Fig. 4 shows a solid infill pattern for bottom and top layers (a), a bridge infill layer (b) and the four infill patterns investigated in detail: concentric (c), gyroid (d), 3D honeycomb (e) and rays (f). All printed layers start with two internal perimeter turns (yellow colored) and one external perimeter turn (orange colored). The infill solid, infill bridge and the infill patterns are colored purple, blue and red respectively. Also shown is the printer head during the infill operations.

Tensile testing

A universal testing machine (UTM), model ME-8244 from Pasco, was used to evaluate the mechanical properties of the PLA printed specimen, as depicted in Fig. 5. This machine has a maximum load capacity of 7100 N and is equipped with PASCO software, which allows control, monitoring, and data recording of the measurement. The tensile tests were conducted at a room temperature of 25 °C and 50% relative humidity, with a jaw displacement speed of 1 mm/min, in accordance with the D638-14 standard. Prior using the UTM, it was calibrated using a calibration rod to adjust the force

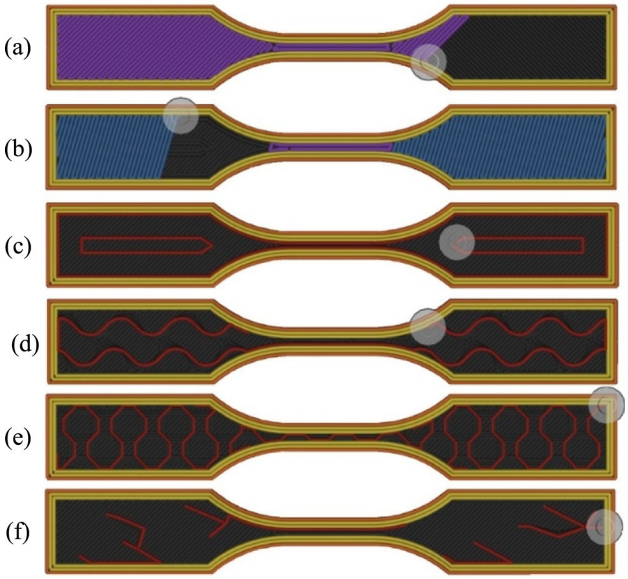

Fig. 4 Layer Infill patterns: **a** solid bottom/top layer, **b** bridging layer, **c** concentric, **d** gyroid, **e** 3D honeycomb and **f** rays

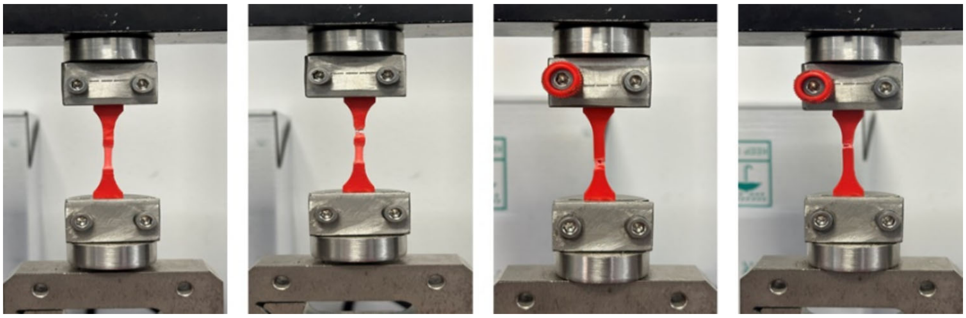

Fig. 5 PLA specimen tensile testing using the ME-8244 UTM according to ASTM D638-14 standard

measured by the load cell. To ensure repeatability of results, special cares were taken to hold securely the upper and lower jaws and align the long axis of the specimen with the jaws before each test. Subsequently, each specimen was tested until the failure occurred. Figure 5 also shows four specimens during the tensile test at failure event.

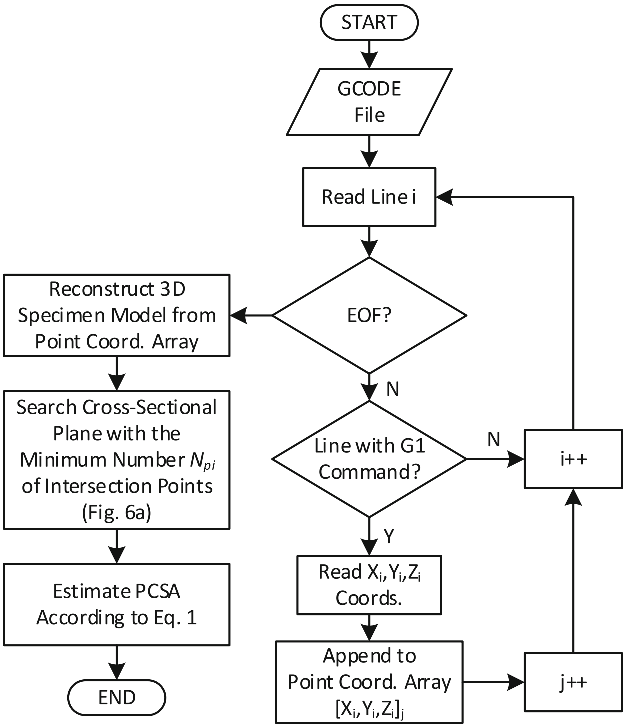

Fig. 6 GCODE file decoding, 3D model reconstruction and PCSA estimation

Data processing

A procedure has been implemented to estimate the cross-sectional areas of ASTM D638 Type-V standard specimens, which were printed using various infill patterns. This procedure specifically aims to identify the minimum cross-sectional area within the gauge zone of the specimen, theoretically corresponding to the specimen's weakest point. The estimation involves analyzing the path traversed by the extruder during the 3D printing process, which is encoded in a GCODE format file.

The initial step of the procedure consists of reading and processing line by line the GCODE file of selected infill pattern to obtain the X, Y, and Z coordinates of points for building linear trajectories (Fig. 6). These line segments are then utilized to reconstruct the 3D model of the object, as depicted in Fig. 7. Following this, the procedure calculates intersections between these line segments and a cross-sectional plane, yielding a set of intersection points. The analysis proceeds along the specimen's gauge length of 7.62 mm, as stipulated by the ASTM D638-14 standard, to locate the position with the minimum number of intersection points, illustrated in Fig. 7a. By employing a predefined step size for the displacement plane, the procedure evaluates intersection points at each step for both the selected model and a model assuming solid infill. The Proportional Cross-Sectional Area (PCSA) is determined by tracking the intersection points where the print paths intersect a transverse plane, which traverses the gauge length of the specimen in defined steps. For each positional step, the number of intersections, N_{pi}, on the targeted infill model and N_{ps} on a solid infill reference model are recorded. The PCSA is then derived from Eq. (1):

$$PCSA = R_{LPI} \cdot S = \frac{N_{pi}}{N_{ps}} \cdot S \tag{1}$$

where, R_{LPI} (Line-Plane Intersection Points Ratio) quantifies the relative density of intersection points between the chosen model and a solid baseline, and S is the calculated cross-sectional area based on the specimen's thickness and width. This approach facilitates a dynamic evaluation of the structural integrity across varying infill configurations, accurately mirroring the mechanical potential of the 3D-printed parts.

For clearer illustration, Fig. 7a depicts four intermediate layers of a gyroid patterned model with intersections marked in red. The gauge length and corresponding cross-sectional plane are delineated in pink and red, respectively, in Fig. 7b. Figure 8a and b provide a visual comparison using a solid

Fig. 7 **a** Intermediate layers of a reconstructed 3D model from a GCODE file and **b** a layer top view

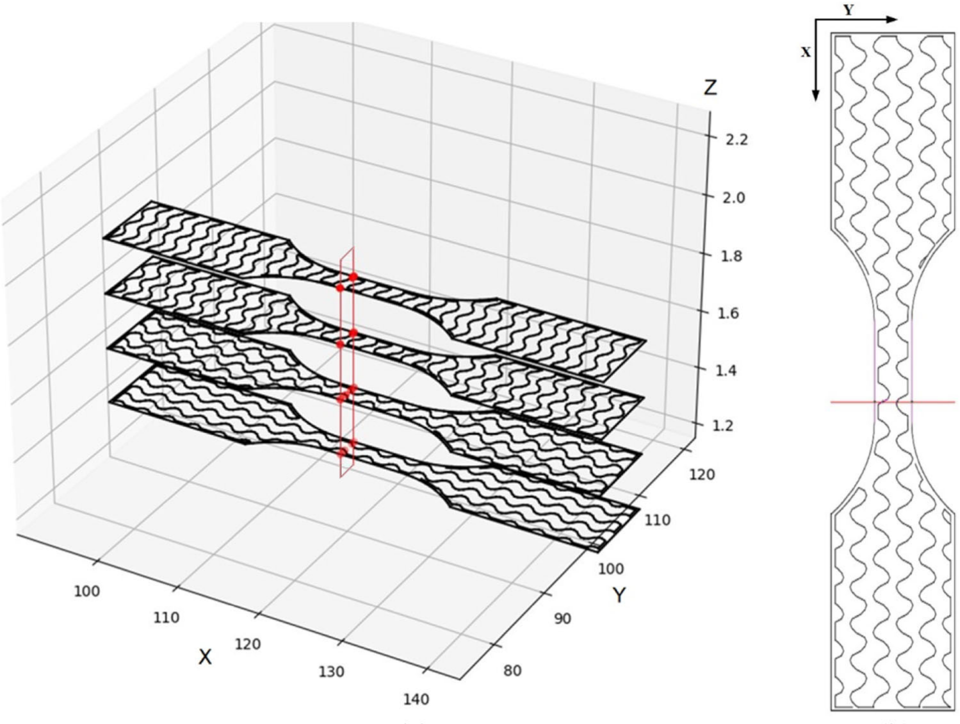

(a) (b)

Fig. 8 **a** Gauge length cross-sectioned and **b** resulting intersection points in a specimen with solid infill pattern

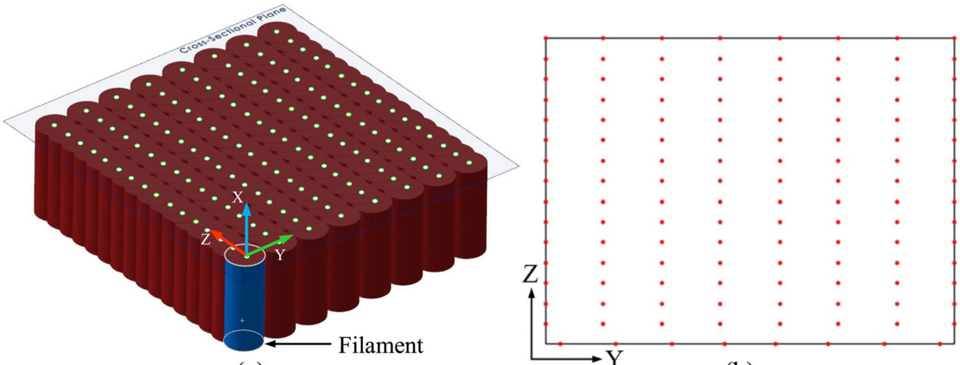

(a) (b)

infill model, demonstrating the intersection points at a typical gauge length where $N_{ps} = N_{pi} = 128$, thereby establishing a reference for comparison.

Results and discussion

Gauge length cross-sectional results

Thickness and width measurements were conducted at the center of gauge length of a specified number, N, of specimens, each featuring different infill patterns. Table 3 shows the average (Avg), standard deviation (Std), minimum value (Min), and maximum value (Max) recorded for both the specimen width and thickness. Additionally, the table lists the cross-sectional area, S, as the product the average width and thickness. This calculated area, 10.572 mm^2 will be used in subsequent calculations of the PCSA value.

The GCODE files for each type of infill pattern were processed to obtain the intersection points of the filaments with the cross-sectional plane, using the MATLAB programming platform. The step size for the displacement plane was set to 0.1 mm.

Figure 9 shows the results of processing the GCODE file for the four infill patterns: concentric, gyroid, 3D honeycomb, and rays. For better visualization, an intermediate layer was selected for each infill pattern. The region corresponding to the gauge length is marked in pink, and the position of the cross-sectional plane with the minimum cross-sectional area of the whole specimen is highlighted in red.

Table 3 Specimen thickness and width statistics

N	Thickness, T (mm)				Width, W (mm)				S (mm^2)
	Avg	Std	Min	Max	Avg	Std	Min	Max	Avg
20	3.02	0.05	2.92	3.15	3.50	0.03	3.40	3.59	10.572

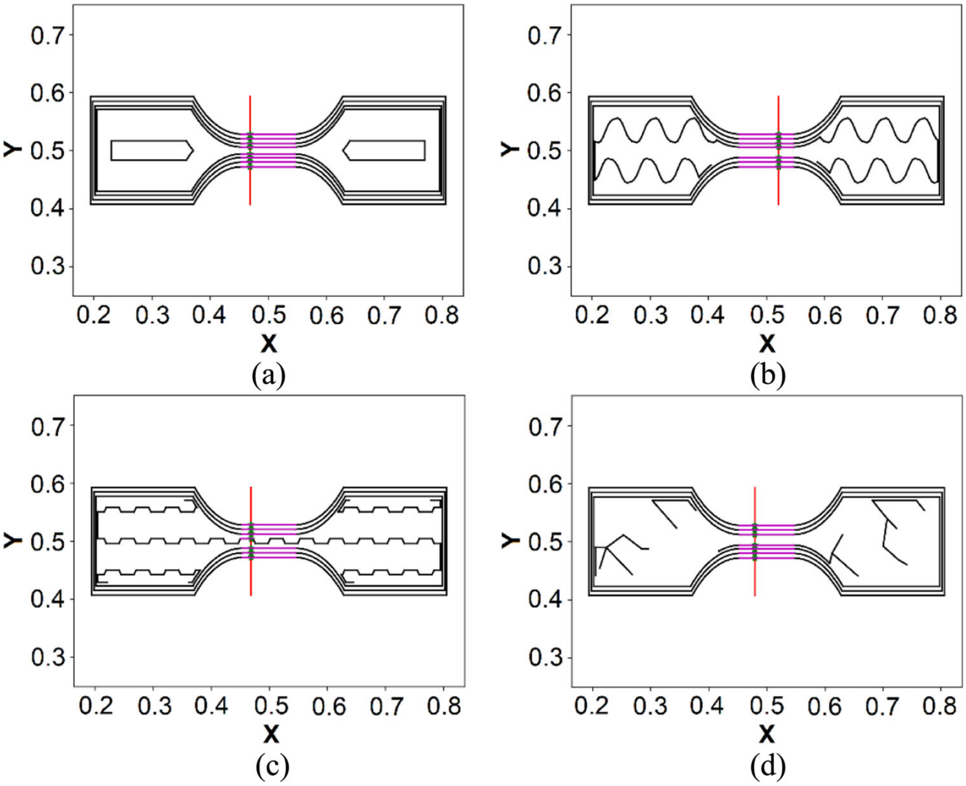

Fig. 9 Minimum cross-sectional area found for infill patterns: **a** concentric, **b** gyroid, **c** 3D honeycomb, and **d** rays

Figure 10 shows the intersection points for these cross-sectional planes across the four infill patterns. It is observed that the position of the cross-sectional plane that determines the minimum area varies in each infill pattern (Fig. 9) as well as the position of the intersection points (Fig. 10). It can also be seen the great void left by the lack of intersection points in each infill pattern because there being no paths of filaments passing through that area (Fig. 10; void regions marked with green dashed line). Regarding what happens along the whole gauge length, a more detailed analysis is necessary.

A total of 77 intersections of plane have been obtained setting 0.1 mm step for the displacement of the plane. Figure 11 shows a radar graph that represents the R_{LPI} value relative to the position of the cutting plane used for its calculation and for each of the infill patterns. The R_{LPI} is expressed as a percentage and the position in millimeters setting the origin to the left side of the specimen gauge length.

Analyzing the radar graph (Fig. 11), great variability is observed in the R_{LPI} values of the different infill patterns as a result of the different trajectories of the line segments of each pattern as they pass through the calibrated length of the specimen. Some of them show drastic changes in their values (Archimedean chords, octagram spiral, stars, honey comb, aligned rectilinear, rectilinear, grid, and triangles).

The statistical values of the line-plane intersection points relation, R_{LPI}, and PCSA value are also shown in Table 4 revealing variations, between 88.46 and 99.67%, for the R_{LPI} value. The variability can be verified quantitatively by the standard deviation values. To easily compare the R_{LPI} values between different infill patterns, a bar chart has been made that shows the average and standard deviation values (Fig. 12).

Four representative infill patterns were selected for a detailed study of their impact on the mechanical properties of the specimens. These patterns were classified into four equally distributed groups based on their average R_{LPI} values: high (from 96.86 to 99.67%: concentric and triangles), medium–high (from 91.26 to 94.06%: Hilbert curve and 3D honeycomb), low (from 88.46 to 91.26%: rays and stars), and medium–low (remaining patterns) (Fig. 12). From

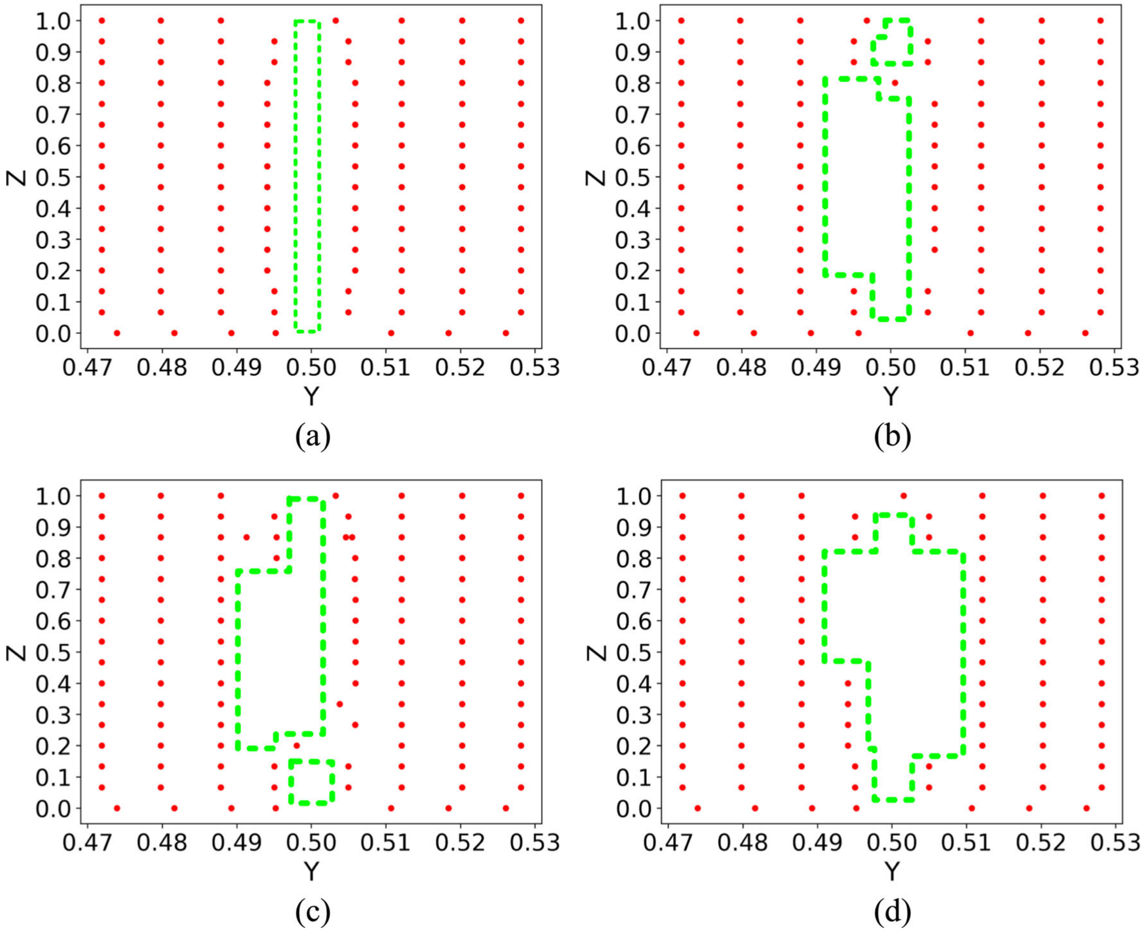

Fig. 10 Intersection points (red colored) found at minimum cross-sectional area and void regions (green colored dashed regions) for different infill patters: **a** concentric, **b** gyroid, **c** 3D honeycomb, and **d** rays (Color figure online)

each group, one infill pattern was chosen for further analysis, specifically those with a low standard deviation (below 1.5%) to ensure stability in the R_{LPI} values along the gauge length. As a result, the concentric, rays, gyroid, and 3D honeycomb patterns were chosen for this expanded analysis.

Table 4 details the statistical values of R_{LPI}, showing that the concentric pattern approximates the maximum theoretical value most closely, with averages around 99.67% along the gauge length, while the lowest average corresponds to the rays at approximately 88.46%. The other patterns display averages of about 94.63% for 3D honeycomb and 92.59% for gyroid. Variability in R_{LPI} values along the gauge length is evident, as illustrated in Fig. 13. This variability is more pronounced in the rays and gyroid patterns, with standard deviations of 1.31% and 1.27% respectively, less pronounced in the 3D honeycomb at 1.08%, and least in the concentric pattern at 0.63%. Additionally, Table 4 provides the estimated average, standard deviation, minimum, and maximum cross-sectional area along the gauge length for each infill pattern.

The radar graph complements the statistical results by providing additional significant information. It demonstrates that multiple cross-sectional planes along the gauge length can exhibit minimum values of R_{LPI} and area. This analysis helps identify positions within the specimen gauge length that may correspond to areas of lower mechanical resistance, potentially indicating the initiation points for premature failure. In the concentric infill pattern, seven positions show minimum values for R_{LPI} and area at 98.43% and 10.40 mm^2, respectively. These minima occur at gauge length positions of approximately 0.75, 1.8, 2.85, 3.9, 4.95, 6.0, and 7.0 mm. For the gyroid infill pattern, the lowest values of 89.84% and 9.49 mm^2 are found at the 6.0 mm position. The 3D honeycomb infill pattern displays several minima with values of 92.96% and 9.82 mm^2 at positions 0.05, 0.75, 1.8, 2.85, 3.9, 4.95, 6.0, and 7.0 mm. Meanwhile, values of 85.93% and 9.08 mm^2 are located at 1.8, 2.85, and 3.9 mm in another pattern. When comparing different infill patterns, certain similarities are noted in the locations of their minimum values. The most striking example is between the concentric and 3D honeycomb infills, where seven coinciding points are identified (0.75, 1.8, 2.85, 3.9, 4.95, 6.0, and 7.0 mm).

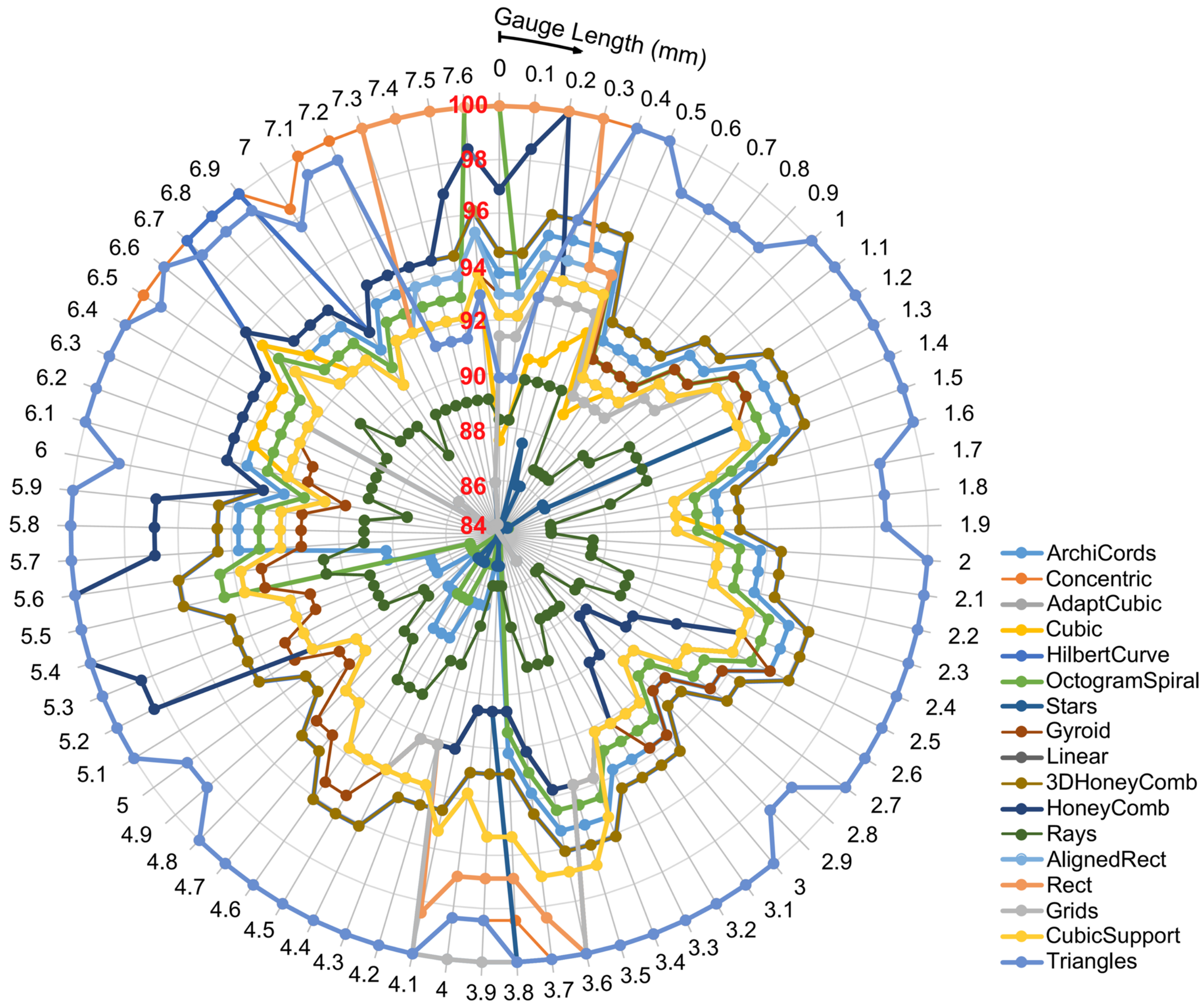

Fig. 11 R_{LPI} (red colored label) versus cross-sectional plane position over gauge length for each infill pattern (Color figure online)

In the analysis of infill pattern performance, particularly concerning structural integrity, the concentric, gyroid, 3D honeycomb, and rays patterns were strategically chosen based on their distinct mechanical behaviors and load distribution characteristics, which are crucial for practical applications. For instance, the concentric pattern is particularly noteworthy for its ability to distribute stress evenly across the printed part, enhancing durability and resistance under load. This pattern performs optimally in terms of yield strength and resilience, making it suitable for applications requiring high mechanical stability. Studies such as those by Birosz et al. (2022) and De Bernardez et al. (2023) have highlighted how variations in geometry—such as the uninterrupted lines of the concentric pattern—contribute significantly to performance by minimizing stress concentrations and optimizing load paths within the structure. These characteristics are crucial for predicting and enhancing the functionality of 3D-printed components under real-world conditions, underscoring the importance of tailored infill configurations to meet specific mechanical demands.

Mechanical properties from stress–strain curves

The mechanical properties of the four selected infill patterns were obtained following the guidelines and testing procedures established by the standard ASTM D-638-14, which is widely recognized for assessing the mechanical properties of polymeric materials. While these tests provide fundamental insights into the material behaviors under tensile stress, we acknowledge the limitations of not examining other types of loading conditions. Future studies should indeed expand the scope of mechanical integrity assessments to include a variety of loading conditions such as compressive, flexural, and/or impact tests. Such investigations would offer a more

Table 4 PCSA statistics for each infill pattern

Infill pattern	R_{LPI} (%)				PCSA (mm^2)			
	Avg	Std	Min	Max	Avg	Std	Min	Max
Archimedean chords	92.20	3.19	85.15	95.31	9.74	0.33	9.00	10.07
Concentric	99.67	0.63	98.43	100	10.53	0.06	10.40	10.53
Adaptative cubic	92.69	1.48	90.62	96.87	9.79	0.15	9.58	10.24
Cubic	92.15	1.40	87.50	95.31	9.74	0.14	9.25	10.07
Hilbert curve	94.84	1.50	92.96	100	10.02	0.15	9.82	10.57
Octagram spiral	91.60	3.70	83.59	100	9.68	0.39	8.83	10.57
Stars	89.91	4.35	82.81	100	9.50	0.46	8.75	10.57
Gyroid	92.59	1.27	89.84	95.31	9.78	0.13	9.49	10.07
Line	92.28	1.08	90.62	93.75	9.75	0.11	9.58	9.91
3D honey comb	94.63	1.08	92.96	96.09	10.00	0.11	9.82	10.15
Honey comb	93.48	2.76	88.28	100	9.88	0.29	9.33	10.57
Rays	88.46	1.31	85.93	90.62	9.35	0.13	9.08	9.58
Aligned rectilinear	93.08	2.33	90.62	100	9.84	0.24	9.58	10.57
Rectilinear	93.54	2.88	90.62	100	9.88	0.30	9.58	10.57
Grid	91.59	3.86	82.81	100	9.68	0.40	8.75	10.57
Support cubic	92.69	1.48	90.62	96.87	9.79	0.15	9.58	10.24
Triangles	98.79	2.49	89.84	100	10.44	0.26	9.49	10.57

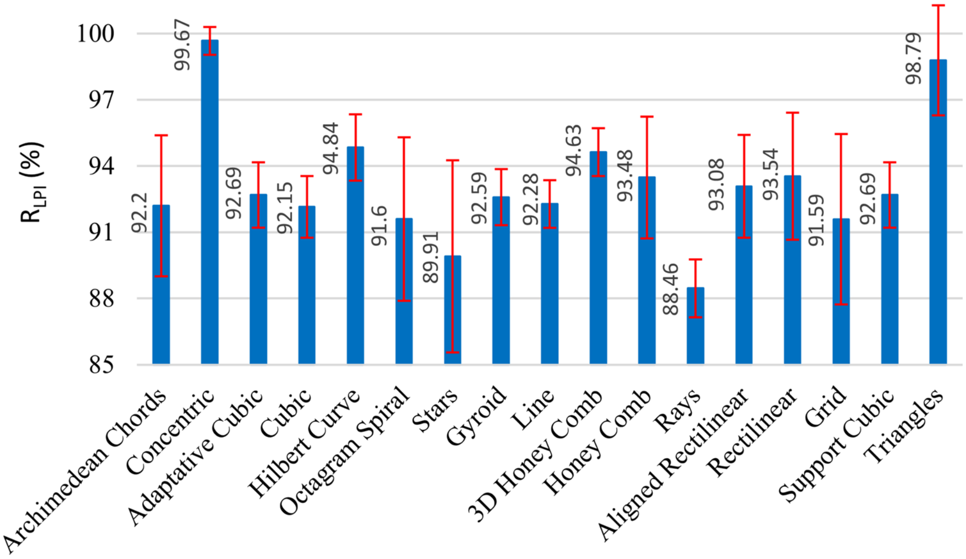

Fig. 12 Bar chart for R_{LPI} statistical values of infill patterns (average and standard deviation red mark) (Color figure online)

complete validation of the suitability of different infill patterns for varied applications, particularly in industries where materials are subject to multi-axial stresses. In the case of the tensile stress, expressed in MPa, is has divided the load sustained by the specimen (in newtons) by the minimum cross-sectional area (in square millimeters) identified within the gauge length. This minimum area is detailed in the Table 4 for each infill patterns. The strain was determined by dividing the length displacement obtained in the specimen by its original gauge length (G = 7.62 mm) and is expressed as a percentage. The elastic modulus, E, was calculated from the slope of the regression line drawn through the initial points of the stress–strain curve, which range from the origin of the curve to a point defined by a secant modulus of 2% strain. Since an extensometer is not used to measure the Young's modulus, it may contain inaccuracies by including UTM axial deformation or displacements of the clamping jaws. Yield strength, σ_y, was calculated from the stress value at the intersection of the stress–strain curve and a line parallel to the initial tangent of the cure, offset by 0.2% strain

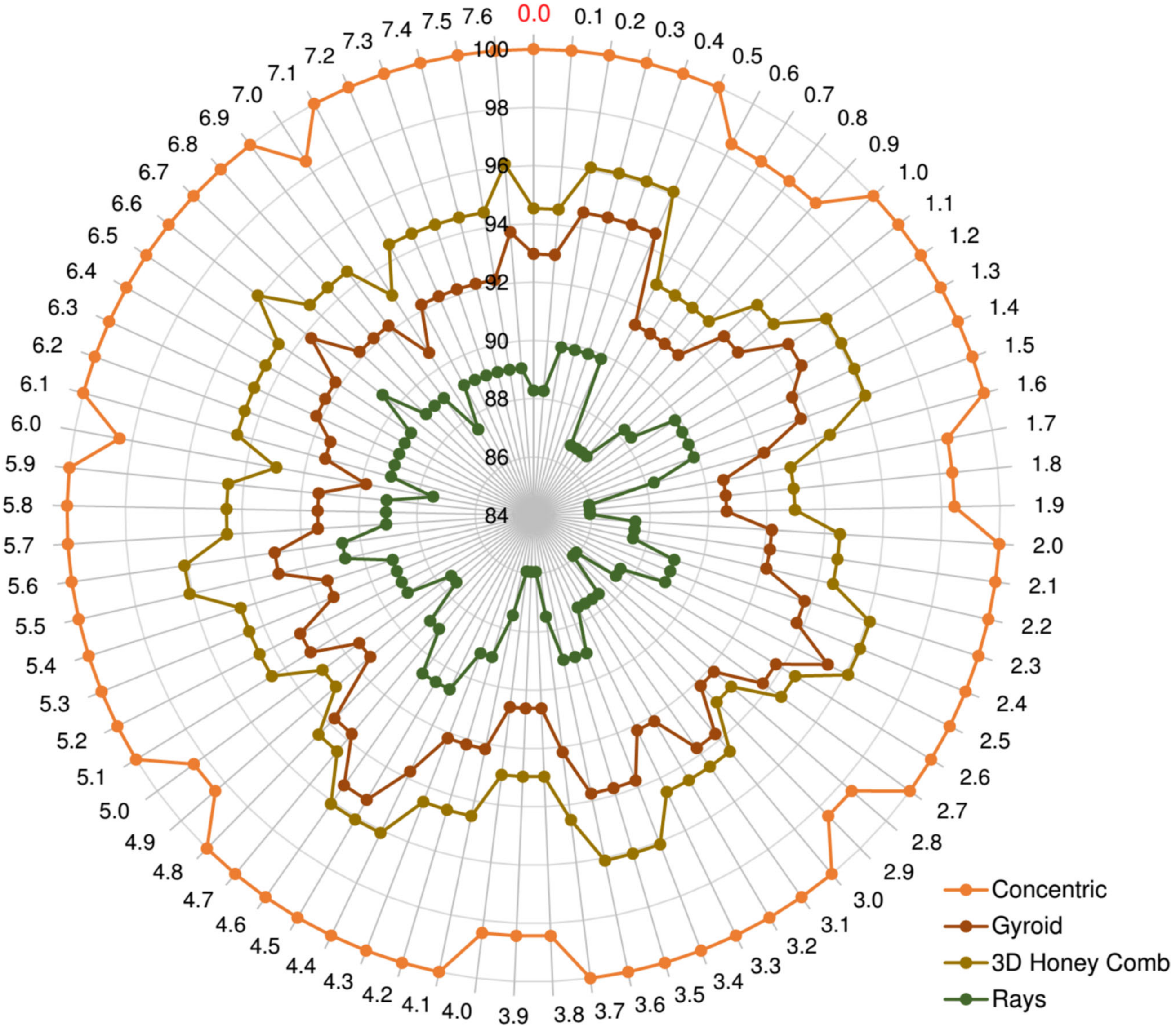

Fig. 13 R_{LPI} versus cross-sectional plane position over gauge length for selected infill pattern

to the right. Ultimate tensile strength, σ_u, tensile strength at break, σ_b, and ductility, δ, were also derived from the stress–strain curve. Finally, the modulus of resilience, U_R, and modulus of toughness, U_T, both expressed in MJ/m^3, were calculated based on the areas under the respective portions of the stress–strain curve.

Table 5 presents summary statistics of the mechanical properties for each of the infill patterns, reporting both the average and standard deviation. The total number of specimens used for statistical analysis was 45, 40, 38, and 39 for the concentric, gyroid, 3D honeycomb, and rays infill patterns, respectively. The stress–strain curves for all specimens within each infill pattern are also depicted in Fig. 14.

The average values of the modulus of elasticity are notably similar for the gyroid and 3D honeycomb patterns, at 705.4 MPa and 705.2 MPa respectively, compared to the rays and concentric patterns, which are lower at 679.3 MPa and 665.1 MPa. These two patterns also show greater variability in this property, with standard deviations of 22.3 MPa for concentric and 23.2 MPa for 3D honeycomb. The yield strength across all four patterns shows a consistent average around 23 MPa, though variability is significant. Tensile strength and modulus of resilience are uniformly recorded at approximately 46 MPa and 0.44 MJ/m^3, respectively, across the patterns. However, the tensile strength at break, ductility, and modulus of toughness display higher variability, as evidenced by the differing behaviors in the plastic deformation regime of the stress–strain curves depicted in Fig. 14.

A deeper analysis of the stress–strain curves reveals substantial differences in the plastic regime, even within each

Table 5 Mechanical properties summary statistic for infill patterns (total, not classified)

Infill Pattern	N	E (MPa)		σ_y (MPa)		σ_u (MPa)		σ_b (MPa)		δ (%)		U_R (MJ/m^3)		U_T (MJ/m^3)	
		Avg	Std	Avg	Std	Avg	Std	Avg	Std	Avg	Std	Avg	Std	Avg	Std
Concentric	35	665.1	22.3	23.1	2.3	44.7	1.4	2.8	4.8	61.2	31.5	0.44	0.09	17.4	9.5
Gyroid	40	705.4	14.2	22.9	1.0	46.5	1.4	1.6	3.8	47.8	30.3	0.41	0.03	13.4	8.6
3D Honeycomb	38	705.2	23.2	23.1	1.3	45.3	1.4	0.8	1.7	36.7	13.3	0.42	0.04	11.7	7.0
Rays	39	679.3	14.9	23.5	1.0	46.9	1.6	2.5	3.1	44.2	8.8	0.41	0.03	11.0	2.3

E, σ_y, σ_u, σ_b, δ, U_R, and U_T are the modulus of elasticity, yield strength, ultimate tensile strength, tensile strength at break, ductility, and resilience and toughness modulus, respectively

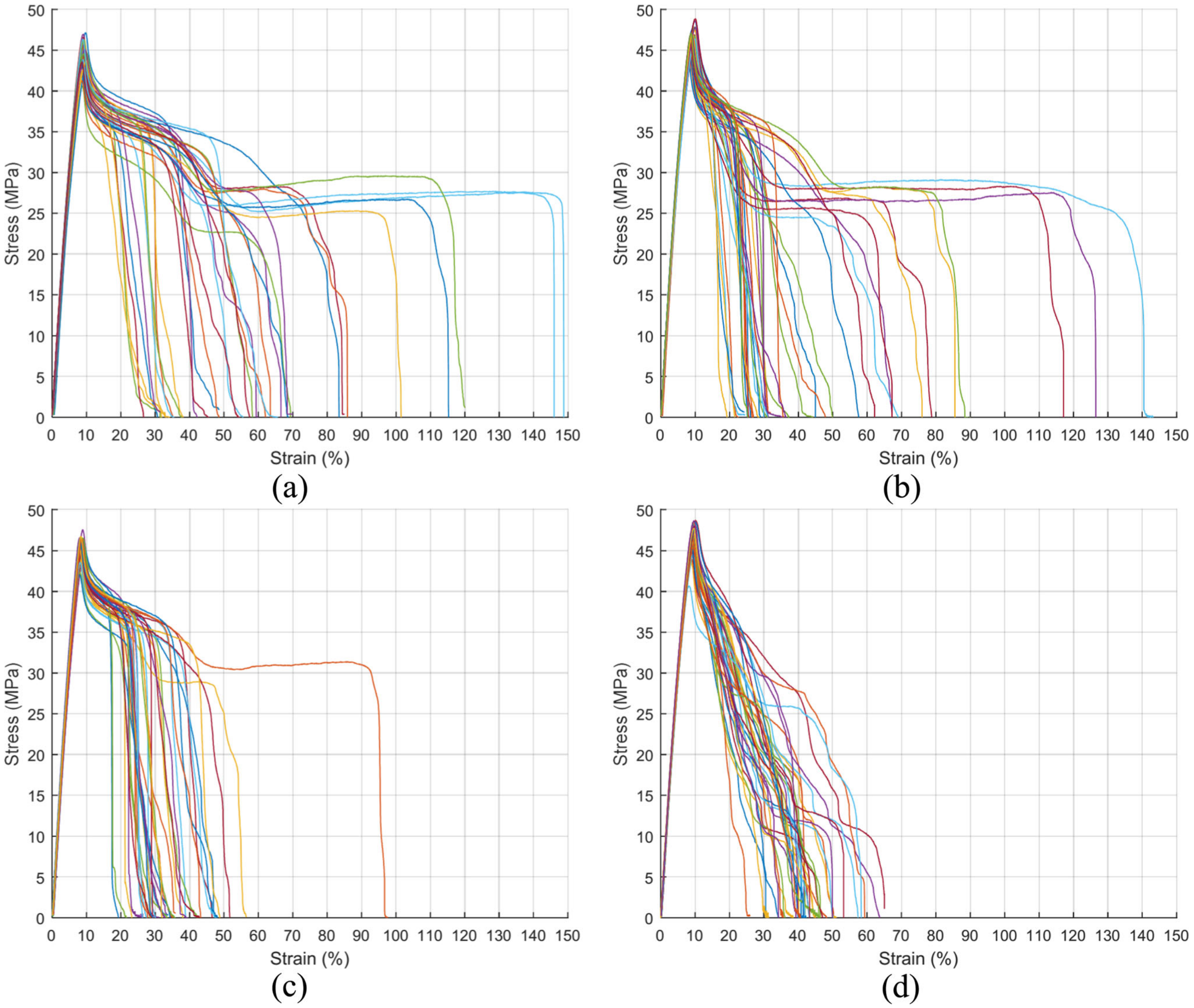

Fig. 14 Stress–strain curves for infill patterns: **a** concentric, **b** gyroid, **c** 3D honeycomb and **d** rays

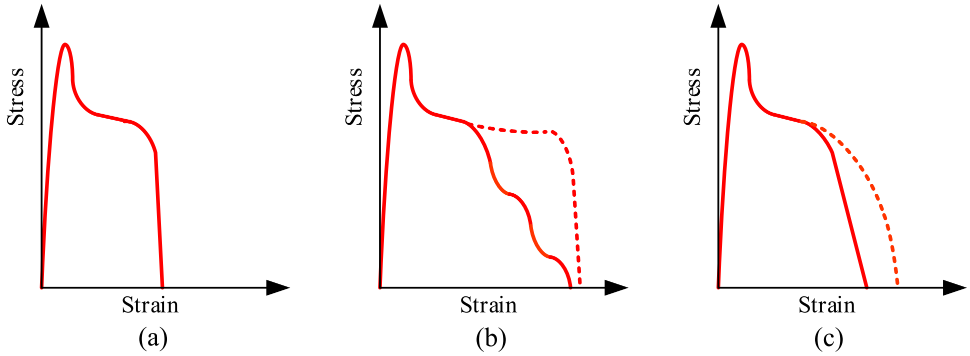

Fig. 15 **a** Fast, **b** staggered, and **c** progressive failure curve shapes

infill pattern. Variability in the properties associated with this regime stems from diverse behaviors observed during testing. Some specimens reach failure quickly (Fig. 15a), others fail in a staggered manner (Fig. 15b), and some show progressive failure (Fig. 15c). Notably, in the second scenario, strain hardening (dashed line in Fig. 15b) has been observed in curves from concentric, gyroid, and 3D honeycomb patterns, even after the tensile strength point was exceeded (Fig. 14a, Fig. 14b, and Fig. 14c). To reduce variability in the statistics and enhance the clarity of the stress–strain curves, the data have been categorized into three distinct groups as previously mentioned: relatively fast failure (Group I), staggered failure (Group II), and progressive failure (Group III).

Figures 16, 17, and 18 display the stress–strain curves classified according to these groups. Tables 6, 7, 8, and 9 summarize the mechanical properties statistics for each infill pattern, categorized by group. Figure 18 shows curves where failure occurs progressively, a behavior specifically noted in the concentric and gyroid patterns, and most commonly observed in the rays pattern. In the latter, a slightly stepped behavior is evident, though it consistently follows a declining trend in deformation until failure (Fig. 18c). The rays pattern exhibits a ductility of 41.2% and a modulus of toughness of 10.3 MJ/m^3, as listed in Table 9 (Group III). These ductility values are comparable to those of the concentric pattern, while the modulus of toughness is slightly lower than those observed in the concentric and 3D honeycomb patterns within Group I (Tables 6, 7, and 8).

Figure 19 displays bar charts with error red marks for each mechanical property derived from Tables 6, 7, 8, and 9. Each chart represents the average value of a mechanical property for each infill pattern, categorized by group. The modulus of elasticity (Fig. 19a) shows significant variations across the infill patterns. Among the four patterns, the gyroid and 3D honeycomb exhibit the highest values, followed by the rays, with the concentric pattern showing the lowest. This greater stiffness of the gyroid and 3D honeycomb patterns could be caused because of having a greater interlocking of the filaments within the layer and between the different infill layers. Likewise, the small differences between the three groups could be related to the strength of the bond between filaments. No significant differences are observed between different groups within the same pattern. Regarding yield strength (Fig. 19b), all patterns display similar values, although the greatest discrepancies are noted between the concentric and the rays patterns. A slight decrease in values is observed for the concentric and gyroid patterns when comparing Group I to Group II. As for ultimate tensile strength (Fig. 19c), the gyroid and rays patterns exhibit the highest values among all patterns, followed by the 3D honeycomb and concentric patterns. Again, no significant differences are detected between different groups of the same pattern. Ductility (Fig. 19d) varies significantly between groups, particularly between Groups I and II for the concentric and gyroid patterns, where values practically double for the concentric and triple for the gyroid. This trend correlates with observations from the stress–strain curves (Figs. 16 and 17). The increase in ductility can be attributed to a combination of factors: the load being distributed across a greater number of filaments and the strong bond between these filaments. In this context, the distribution of the load along the gauge length is significant; as the mechanical stability of the specimen improves, the value of this distribution increases.

Concerning the energy absorbed in the elastic regime (modulus of resilience, Fig. 19e), only minor variations are noted between patterns and groups. Comparing these values to the total deformation energy absorbed (modulus of toughness, Fig. 19f) reveals a substantial plastic regime. Figure 19f matches the shape of the ductility bar chart showed in the Fig. 19d, as could be expected. Variations in tensile strength at break values (Fig. 19g) observed in Group II compared to other groups may relate to the slight strain hardening observed in most curves (concentric, gyroid, and 3D honeycomb patterns, but not in the rays pattern), alongside higher levels of ductility.

This research has effectively highlighted the impact of various infill patterns on the mechanical properties of FDM-printed PLA specimens, substantiating the influence of infill configuration on the structural integrity and performance of

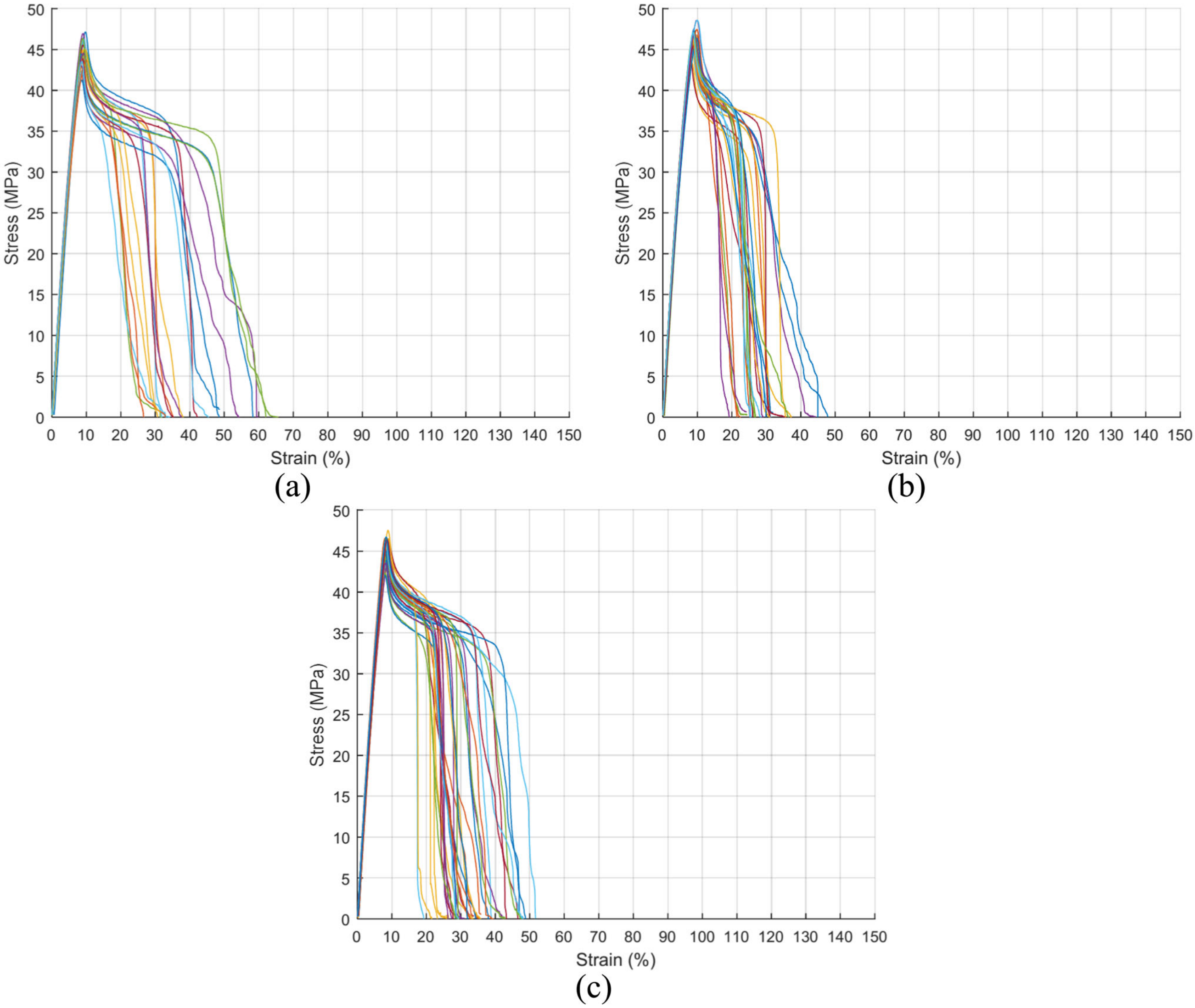

(a) (b) (c)

Fig. 16 Stress–strain curves with relatively fast failure (Group I): **a** concentric, **b** gyroid, and **c** 3D honeycomb infill patterns

3D-printed materials. By systematically analyzing the proportional cross-sectional areas and stress–strain curves, the study has uncovered significant variability in the line-plane intersection points ratio among different infill patterns. This variability not only confirms the crucial role of infill geometry in mechanical performance but also aligns with findings from Sandanamsamy et al. (Sandanamsamy, et al. 2023), who underscored the impact of infill density and raster angle on the tensile strength of printed materials. In recognition of the complexities inherent in 3D printing technologies, this study initially focused on the influence of infill patterns on the mechanical properties of printed objects. However, it is recognized that other significant printing parameters, such as infill density, print speed, and layer height, may interact in ways that substantially affect the final product's structural integrity and strength. Future iterations of this research could employ a comprehensive experimental design using Design of Experiments (DOE) methodologies. This approach could allow a systematic exploration of these parameters and their interactions, providing deeper insights into the optimization of 3D printing settings for enhanced material performance. Such studies are crucial for advancing our understanding of how to best leverage 3D printing technology for engineering applications requiring high reliability and precision.

In particular, the concentric infill pattern showed a higher R_{LPI} value with better performance. This can be attributed to an efficient load distribution throughout the gauge length of the specimen. While it has slightly lower stiffness compared to the other infill patterns, it offers a higher yield strength and greater resilience, resulting in improved mechanical stability and structural integrity within the elastic regime. This better structural integrity along the Y-axis of the specimen could

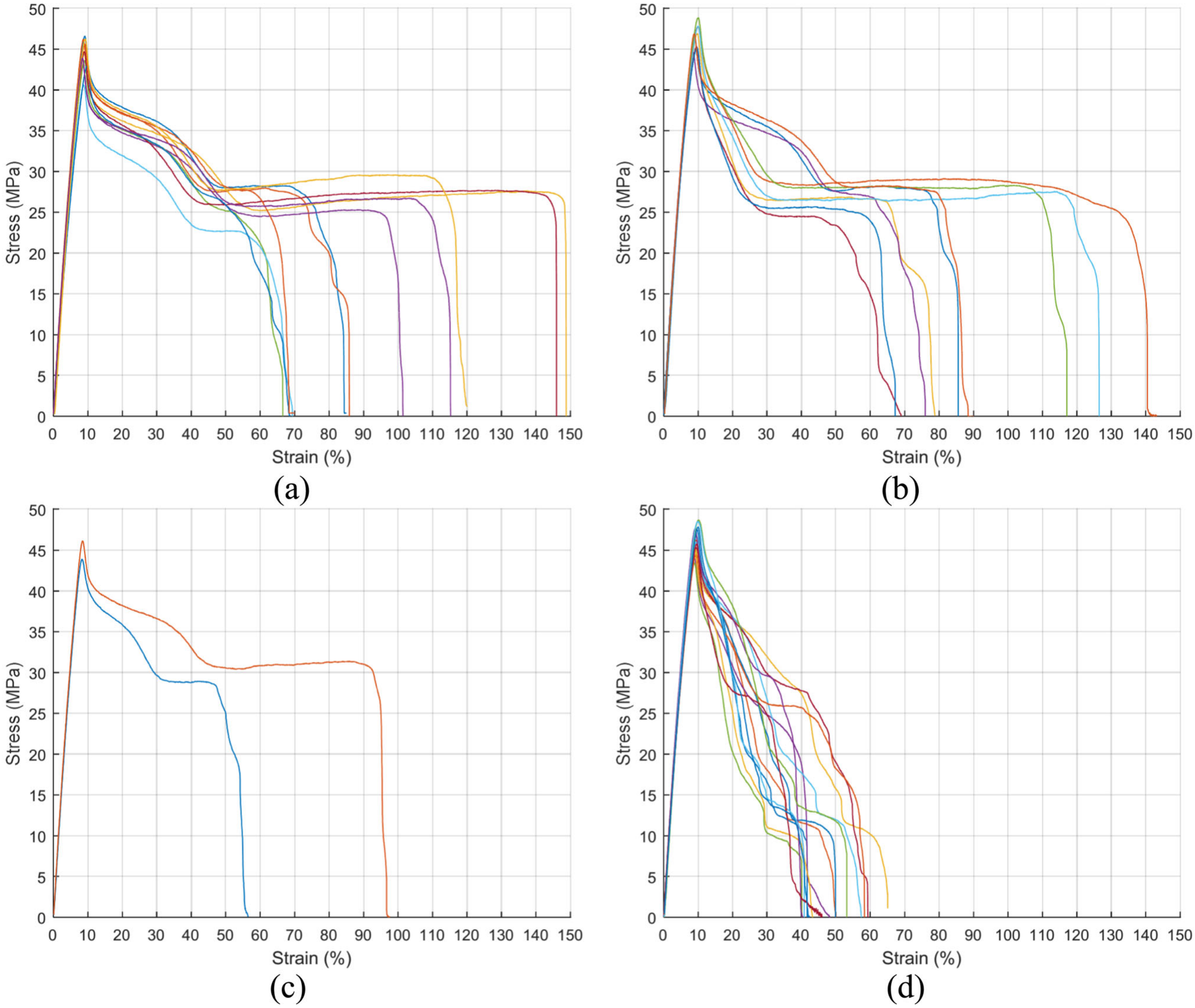

Fig. 17 Stress–strain curves with staggered failure (Group II): **a** concentric, **b** gyroid, **c** 3D honeycomb, and **d** rays infill patterns

be related to the directionality of the infill pattern (direction of the filament orientation) and a more uniform distribution of the material. In addition, this pattern generally exhibits greater ductility and modulus of toughness, which makes it interesting for those applications that require greater deformation absorption. This observation resonates with the work of Garcia et al. (Galina et al., 2016), emphasizing the substantial variations in mechanical properties resulting from changes in layer thickness and deposition parameters. Additionally, our results reflect the broader implications of FDM parameters on material properties as discussed by Wang et al. (Wang et al., 2017) and Vakharia et al. (Vakharia et al., 2021), suggesting that a deeper exploration into infill patterns and material types could enhance the applicability of FDM in industrial applications.

Furthermore, the development of predictive modeling tools to simulate various infill configurations before printing, as proposed by Sandanamsamy et al. (Sandanamsamy, Mogan, et al. 2023), represents a promising avenue for optimizing design and manufacturing processes. Such tools could potentially reduce material waste and enhance the functional performance of 3D-printed parts, making a significant contribution to resource efficiency and cost-effectiveness in additive manufacturing. Moreover, the research conducted herein complements studies such as those by Chawla et al. (Chawla et al., 2021), where the focus was on the mechanical properties of multi-material ABS-based composites. This study extends those findings by providing a more nuanced understanding of how specific infill patterns like gyroid and 3D honeycomb can influence mechanical stability and failure modes, which is crucial for designing components that meet

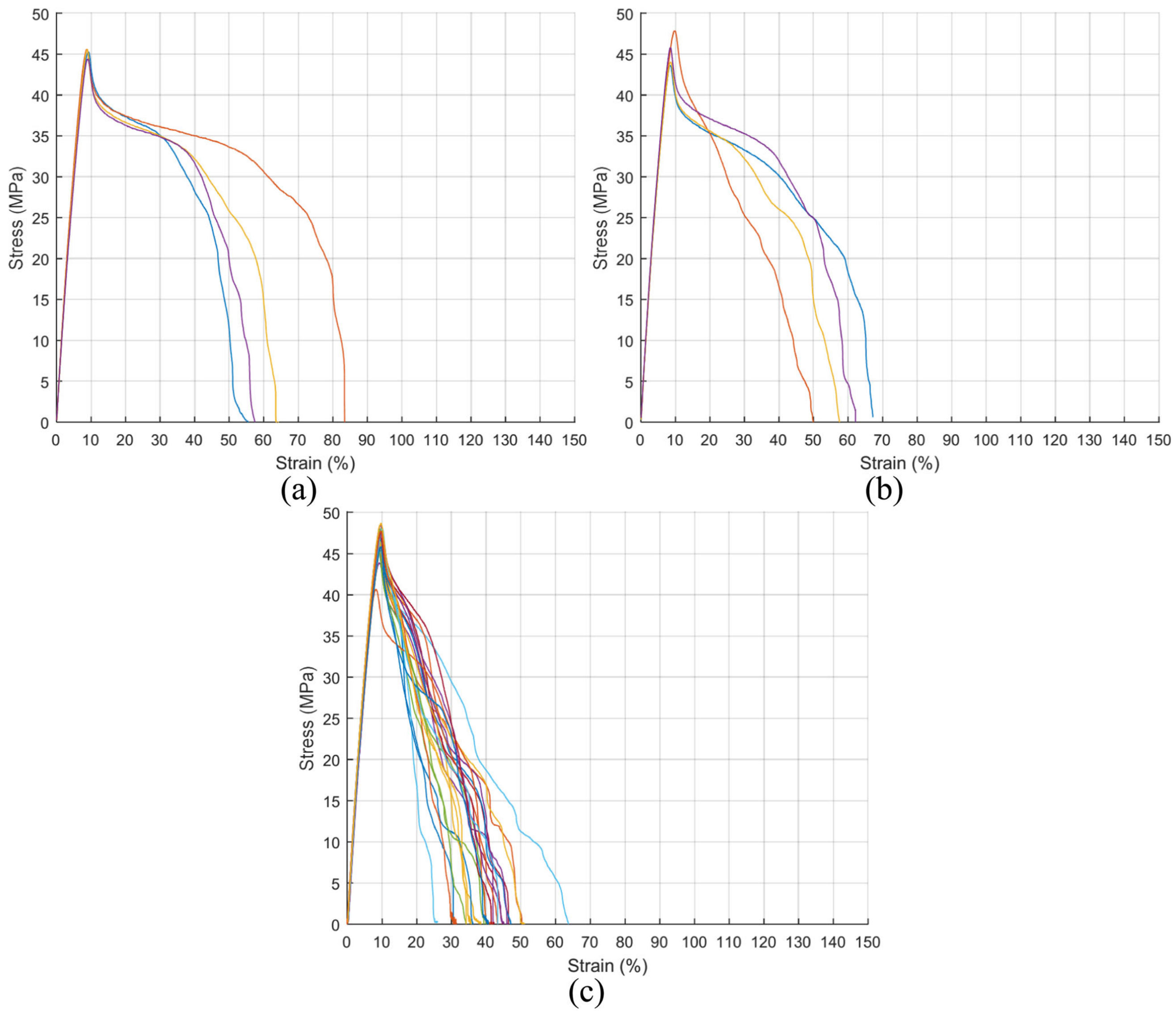

Fig. 18 Stress–strain curves with progressive failure (Group III): **a** concentric, **b** gyroid, and **c** rays infill patterns

Table 6 Summary statistic for concentric infill pattern (by group)

Curve group	N	E (MPa)		σ_y (MPa)		σ_u (MPa)		σ_b (MPa)		δ (%)		$\boldsymbol{U_R}$ (MJ/m^3)		$\boldsymbol{U_T}$ (MJ/m^3)	
		Avg	Std	Avg	Std	Avg	Std	Avg	Std	Avg	Std	Avg	Std	Avg	Std
I	20	668.3	18.0	23.3	2.7	44.7	1.4	0.7	1.3	42.5	11.9	0.45	0.11	11.7	4.0
II	11	656.4	29.6	22.7	1.91	44.7	1.7	7.3	6.2	97.6	30.91	0.42	0.06	28.0	9.11
III	4	673.5	15.9	23.0	1.4	45.4	0.7	2.4	3.0	65.2	12.5	0.42	0.04	19.5	4.6
Total	35	665.1	22.3	23.1	2.3	44.7	1.4	2.8	4.8	61.2	31.5	0.44	0.09	17.4	9.5

Table 7 Summary statistic for gyroid infill pattern (by group)

Curve group	N	E (MPa)		σ_y (MPa)		σ_u (MPa)		σ_b (MPa)		δ (%)		U_R (MJ/m^3)		U_T (MJ/m^3)	
		Avg	Std	Avg	Std	Avg	Std	Avg	Std	Avg	Std	Avg	Std	Avg	Std
I	27	708.6	12.8	23.1	1.1	46.4	1.3	0.3	0.9	30.5	7.2	0.41	0.04	8.6	1.9
II	9	698.4	17.8	22.5	0.8	47.0	1.4	6.0	6.3	94.6	27.3	0.39	0.02	26.7	8.4
III	4	699.2	7.9	22.9	1.0	45.7	2.1	0.6	1.2	59.3	7.3	0.41	0.01	16.4	2.7
Total	40	705.4	14.2	22.9	1.0	46.5	1.4	1.6	3.8	47.8	30.3	0.41	0.03	13.4	8.6

Table 8 Summary statistic for 3D honeycomb infill pattern (by group)

Curve group	N	E (MPa)		σ_y (MPa)		σ_u (MPa)		σ_b (MPa)		δ (%)		U_R (MJ/m^3)		U_T (MJ/m^3)	
		Avg	Std	Avg	Std	Avg	Std	Avg	Std	Avg	Std	Avg	Std	Avg	Std
I	36	706.8	22.6	23.1	1.3	45.4	1.5	0.8	1.7	36.8	13.7	0.42	0.04	11.9	7.2
II	2	696.0	19.8	23.1	2.5	45.0	1.6	0.0	0.0	75.8	30.1	0.42	0.10	23.9	10.4
III	–	–	–	–	–	–	–	–	–	–	–	–	–	–	–
Total	38	701.4	21.2	23.1	1.9	45.2	1.5	0.4	0.8	56.3	21.9	0.42	0.07	17.9	8.8

Table 9 Summary statistic for rays infill pattern (by group)

Curve group	N	E (MPa)		σ_y (MPa)		σ_u (MPa)		σ_b (MPa)		δ (%)		U_R (MJ/m^3)		U_T (MJ/m^3)	
		Avg	Std	Avg	Std	Avg	Std	Avg	Std	Avg	Std	Avg	Std	Avg	Std
I	–	–	–	–	–	–	–	–	–	–	–	–	–	–	–
II	15	678.0	16.0	22.6	1.1	47.1	1.4	4.0	3.6	49.1	8.0	0.40	0.03	12.2	2.6
III	24	680.3	14.6	22.4	1.0	46.9	1.8	1.7	2.4	41.2	7.9	0.41	0.03	10.3	1.8
Total	39	679.3	14.9	23.5	1.0	46.9	1.6	2.5	3.1	44.2	8.8	0.41	0.03	11.0	2.3

specific functional requirements in sectors such as biomedical engineering and aerospace.

Significantly, the results of this study indicate that the gyroid and 3D honeycomb patterns demonstrate lower standard deviations in mechanical properties, suggesting a more consistent behavior under load compared to concentric and rays patterns. The consistency in these patterns can be attributed to their complex internal network which allows for better force absorption and redistribution. This observation aligns with findings from recent studies, such as those by Patel et al. (Patel et al., 2023, 2024) which highlight the role of complex geometrical configurations in improving the isotropic properties of materials, thereby reducing variability in mechanical performance under different loading conditions. These studies emphasize that the continuous fiber paths within such patterns enhance the material's ability to withstand stresses without localized failure, which is crucial for structural applications in aerospace and automotive industries.

Their research is particularly insightful, revealing that patterns like gyroid and honeycomb not only reduce material usage but also enhance the mechanical integrity of the printed structures, with specific infill densities yielding near-solid part strengths. This underscores the importance of strategic infill pattern selection to optimize both the ecological and structural aspects of 3D-printed parts, aligning with broader industry goals of enhancing performance while reducing waste. Their findings support the notion that informed adjustments to infill parameters can significantly influence 3D printing outcomes, which is crucial for industries aiming to integrate more sustainable practices without compromising part functionality. Complementing these findings, the study of Dev and Srivastava (Dev & Srivastava, 2021) revealed that patterns like gyroid and honeycomb not only reduce material usage but also enhance the mechanical integrity of the printed structures, with specific infill densities yielding near-solid part strengths. This underscores the importance of strategic infill pattern selection to optimize both the ecological and structural aspects of 3D-printed parts, aligning with broader

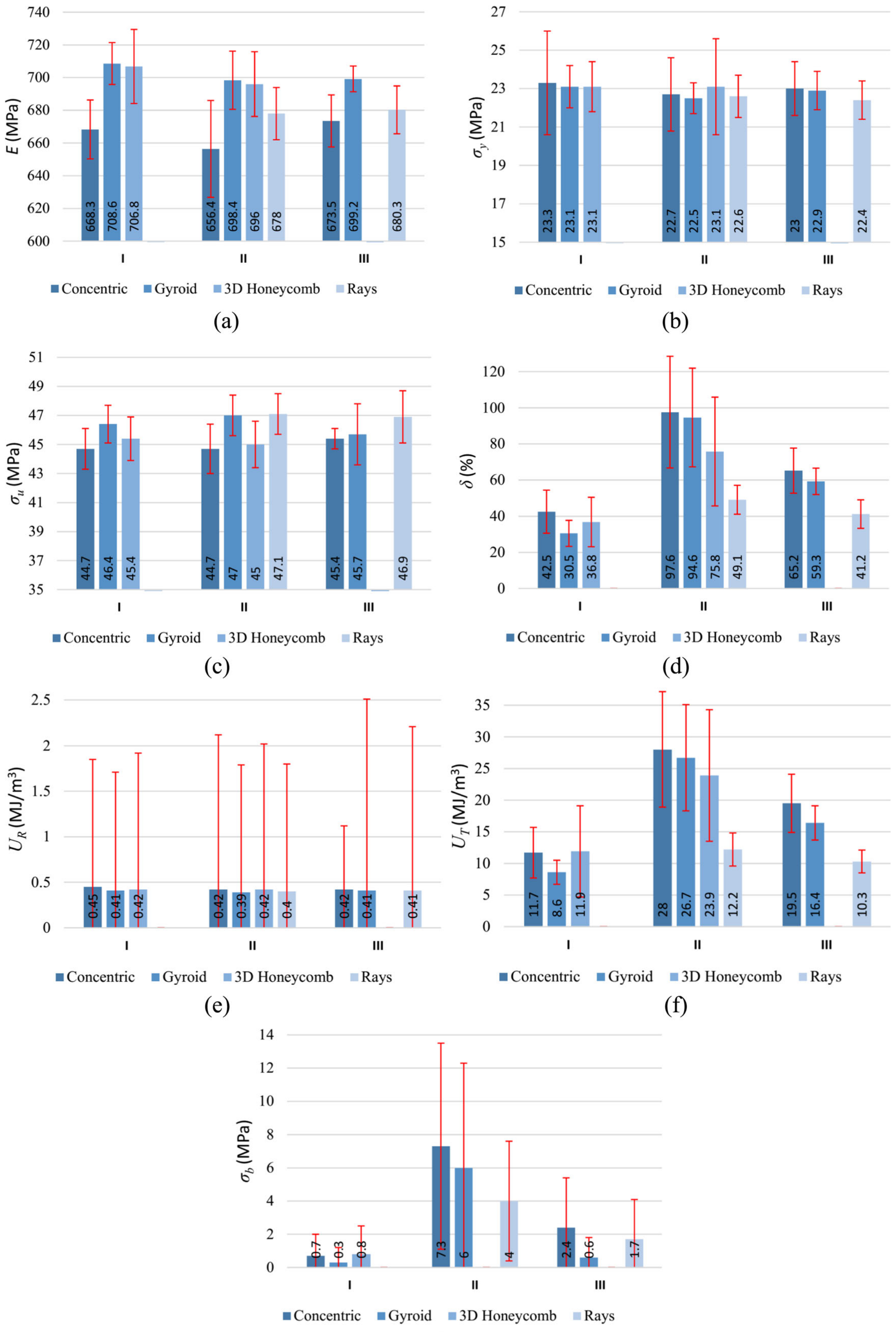

Fig. 19 Average values and deviations (red marked error bar) of the mechanical properties classified by infill pattern and group: **a** modulus of elasticity E, **b** yield strength σ_y, **c** ultimate tensile strength σ_u, **d** ductility δ, **e** modulus of resilience U_R, **f** modulus of toughness U_T, and **g** tensile strength at break σ_b(Color figure online)

industry goals of enhancing performance while reducing waste. Their findings support the notion that informed adjustments to infill parameters can significantly influence 3D printing outcomes, which is crucial for industries aiming to integrate more sustainable practices without compromising part functionality. These findings suggest that further exploration into bio-inspired designs could yield even more efficient material use and strength characteristics, thereby refining this approach to 3D print settings and applications.

The insights gained from this study contribute to a more comprehensive understanding of the dynamics between 3D printing parameters and the mechanical properties of PLA. They underscore the importance of parameter optimization, particularly infill pattern selection, in tailoring the mechanical performance of 3D-printed materials. This research provides a robust foundation for future investigations into the impacts of various infill geometries and material compositions, emphasizing how specific configurations can influence structural integrity and durability. Future research could leverage these findings to explore new materials and composite fabrications, potentially enhancing the capabilities of FDM technology for more demanding industrial applications. Such studies would not only validate the current findings in broader contexts but also open avenues for the application of 3D printing in sectors requiring high-performance materials with precise mechanical properties. This expansion could lead to significant advancements in fields such as aerospace and automotive engineering, where customized material properties are crucial for component reliability and overall system safety.

Conclusions

This research introduced a novel analytical methodology to assess the structural integrity of 3D-printed polylactic acid (PLA) specimens using fused deposition modeling (FDM) technology. The methodology focused on determining the minimum cross-sectional area along the gauge length of the specimens by analyzing the GCODE file to trace the extruder path. This approach pinpointed critical weak points through the calculation of intersection points between the extruder trajectories and a moving transverse plane along the gauge length, yielding an index known as the proportional cross-sectional area (PCSA).

Significant findings from the study include the variability in the line-plane intersection points ratio (R_{LPI}) across different infill patterns, illustrating how the structural characteristics of 3D-printed objects can significantly differ based on the chosen infill geometry. For instance, concentric patterns exhibited enhanced mechanical stability in R_{LPI} value (99.67%), while patterns such as rays displayed potential structural weaknesses (88.46%). The research evaluated four infill patterns concentric, gyroid, 3D honeycomb, and rays and linked these to various mechanical properties derived from stress–strain curves, including modulus of elasticity, yield strength, and ultimate tensile strength.

Minor differences were observed in the mechanical properties within the elastic regime. Both the yield strength and modulus of resilience displayed very similar values across all infill patterns. However, the modulus of elasticity showed that the gyroid and 3D honeycomb patterns exhibited greater stiffness compared to the rays and concentric patterns. Significant differences were noted in the plastic regime. This behavior was categorized into three groups: those with relatively fast failure (Group I), staggered failure (Group II), and progressive failure (Group III). It was observed that the concentric, gyroid, and 3D honeycomb patterns predominantly exhibited rapid failure, with the gyroid pattern showing the least variability. Staggered failure was rare in the concentric and gyroid patterns and exceptional in the 3D honeycomb pattern. In some instances, strain hardening occurred, significantly increasing ductility and the modulus of toughness. Conversely, progressive failure was most commonly seen in the rays pattern, which displayed considerable variability in its ductility and modulus of toughness.

The implications of this study extend broadly, influencing design and manufacturing practices, particularly in sectors where precise material properties are essential, such as biomedical engineering and aerospace. Future research should explore a wider array of infill patterns and diverse materials to expand the applicability of these findings. It is particularly pertinent to examine the relationship between the positions where the minimum RLPI values were identified and the locations of specimen failure during tensile tests. Additionally, there is considerable potential for developing predictive modeling tools that can simulate the behavior of various infill patterns before printing. Such tools could significantly conserve resources and enhance the design process, facilitating the production of more optimized 3D-printed components.

Author contribution Cañero-Nieto, J.M.: Conceptualization, Data curation, Formal analysis, Investigation, Methodology, Project administration, Supervision, Validation, Visualization, Writing-original draft, Writing-review & editing. Campo-Campo, R.J.: Investigation, Methodology, Resources. Díaz-Bolaño, I.B.: Formal analysis, Investigation, Methodology, Project administration, Supervision, Validation, Visualization. Ariza, E.A.: Formal analysis, Investigation, Methodology, Supervision, Validation, Visualization, Writing-original draft, Writing-review & editing. Deluque-Toro, C.E.: Conceptualization, Data curation, Formal analysis, Investigation, Methodology, Project administration, Supervision, Validation, Visualization, Writing-original draft, Writing-review & editing. Solano-Martos, J. F.: Data curation, Formal

analysis, Investigation, Methodology, Resources, Supervision, Validation, Visualization, Writing-original draft.

Funding Open Access funding provided by Colombia Consortium. Open access funding provided by Universidad de Málaga / CBUA.. FONCIENCIAS 2019 (Universidad del Magdalena).

Data availability Data available on request from the authors.

Declarations

Competing interests The authors declare that they have no known competing financial interest or personal relationships that could have appeared to influence the work reported in this paper.

References

ASTM D638. (2014). Standard test method for tensile properties of plastics. *ASTM Standards, 08*, 1–16. https://doi.org/10.1520/D0638-14.1

Birosz, M. T., & Andó, M. (2024). Effect of infill pattern scaling on mechanical properties of FDM-printed PLA specimens. *Progress in Additive Manufacturing, 9*(4), 875–883. https://doi.org/10.1007/s40964-023-00487-8

Birosz, M. T., Ledenyák, D., & Andó, M. (2022). Effect of FDM infill patterns on mechanical properties. *Polymer Testing, 113*(107654), 1–6. https://doi.org/10.1016/j.polymertesting.2022.107654

Cadete, M. S., Gomes, T. E. P., Gonçalves, I., & Neto, V. (2024). Influence of 3D-printing deposition parameters on crystallinity and morphing properties of PLA-based materials. *Progress in Additive Manufacturing, 0123456789*, 1–11. https://doi.org/10.1007/s40964-024-00608-x

Chawla, K., Singh, R., & Singh, J. (2021). Investigations on flexural strength of multi-material ABS based composite specimen fabricated through FDM technique. *Materials Today: Proceedings, 48*, 1346–1351. https://doi.org/10.1016/j.matpr.2021.09.062

De Bernardez, L., Campana, G., Mele, M., Sanguineti, J., Sandre, C., & Mur, S. M. (2023). Effects of infill patterns on part performances and energy consumption in acrylonitrile butadiene styrene fused filament fabrication via industrial-grade machine. *Progress in Additive Manufacturing, 8*(2), 117–129. https://doi.org/10.1007/s40964-022-00316-4

Dev, S., & Srivastava, R. (2021). Effect of infill parameters on material sustainability and mechanical properties in fused deposition modelling process: A case study. *Progress in Additive Manufacturing, 6*(4), 631–642. https://doi.org/10.1007/s40964-021-00184-4

Exley, O., Perera, Y. S., & Abeykoon, C. (2024). Investigation of the effect of the degree of hollowness and internal cavity structure on the mechanical properties of 3D-printed parts. *International Journal of Lightweight Materials and Manufacture, 7*(1), 45–61. https://doi.org/10.1016/j.ijlmm.2023.06.005

Galina, D. M., Garcia, D. P., De Souza, G. G., Resende, R., & Maziero, R. (2016). Caracterización de las propiedades mécanicas de los cuerpos de prueba ABS confeccionados con diferentes parámetros de extrusión vía impresión 3D. *Revista Iberoamericana De Polímeros, 17*(6), 303–309.

Hasan, M. R., Davies, I. J., Pramanik, A., John, M., & Biswas, W. K. (2024). Potential of recycled PLA in 3D printing: A review. *Sustainable Manufacturing and Service Economics, 3*(100020), 1–23. https://doi.org/10.1016/j.smse.2024.100020

Hsueh, M. H., Lai, C. J., Chung, C. F., Wang, S. H., Huang, W. C., Pan, C. Y., et al. (2021). Effect of printing parameters on the tensile properties of 3d-printed polylactic acid (Pla) based on fused deposition modeling. *Polymers, 13*(14), 1–16. https://doi.org/10.3390/polym13142387

Kadhum, A. H., Al-Zubaidi, S., & Abdulkareem, S. S. (2023). Effect of the infill patterns on the mechanical and surface characteristics of 3D printing of PLA, PLA+ and PETG materials. *ChemEngineering*. https://doi.org/10.3390/chemengineering7030046

Kechagias, J., & Zaoutsos, S. (2024). Effects of 3D-printing processing parameters on FFF parts' porosity: Outlook and trends. *Materials and Manufacturing Processes, 39*(6), 804–814. https://doi.org/10.1080/10426914.2024.2304843

Khosravani, M. R., Berto, F., Ayatollahi, M. R., & Reinicke, T. (2022). Characterization of 3D-printed PLA parts with different raster orientations and printing speeds. *Scientific Reports, 12*(1), 1–9. https://doi.org/10.1038/s41598-022-05005-4

Morettini, G., Palmieri, M., Capponi, L., & Landi, L. (2022). Comprehensive characterization of mechanical and physical properties of PLA structures printed by FFF-3D-printing process in different directions. *Progress in Additive Manufacturing, 7*(5), 1111–1122. https://doi.org/10.1007/s40964-022-00285-8

Mushtaq, R. T., Wang, Y., Bao, C., Rehman, M., Sharma, S., Khan, A. M., et al. (2024). Maximizing performance and efficiency in 3D printing of polylactic acid biomaterials: Unveiling of microstructural morphology, and implications of process parameters and modeling of the mechanical strength, surface roughness, print time, and print energy. *International Journal of Biological Macromolecules, 259*(129201), 1–18. https://doi.org/10.1016/j.ijbiomac.2024.129201

Özsoy, K., Erçetin, A., & Çevik, Z. A. (2021). Comparison of mechanical properties of PLA and ABS based structures produced by fused deposition modelling additive manufacturing. *European Journal of Science and Technology, 27*, 802–809.

Patel, K. S., Shah, D. B., Joshi, S. J., Aldawood, F. K., & Kchaou, M. (2024). Effect of process parameters on the mechanical performance of FDM printed carbon fiber reinforced PETG. *Journal of Materials Research and Technology, 30*, 8006–8018. https://doi.org/10.1016/j.jmrt.2024.05.184

Patel, K. S., Shah, D. B., Joshi, S. J., & Patel, K. M. (2023). Developments in 3D printing of carbon fiber reinforced polymer containing recycled plastic waste: A review. *Cleaner Materials, 9*, 100207. https://doi.org/10.1016/j.clema.2023.100207

Pazhamannil, R. V., Govindan, P., Edacherian, A., & Hadidi, H. M. (2022). Impact of process parameters and heat treatment on fused filament fabricated PLA and PLA-CF. *International Journal on Interactive Design and Manufacturing, 18*(4), 2199–2213. https://doi.org/10.1007/s12008-022-01082-x

Rodríguez-Reyna, S. L., Mata, C., Díaz-Aguilera, J. H., Acevedo-Parra, H. R., & Tapia, F. (2022). Mechanical properties optimization for PLA, ABS and nylon + CF manufactured by 3D FDM printing. *Materials Today Communications, 33*, 1–12. https://doi.org/10.1016/j.mtcomm.2022.104774

Sandanamsamy, L., Harun, W. S. W., Ishak, I., Romlay, F. R. M., Kadirgama, K., Ramasamy, D., et al. (2023a). A comprehensive review on fused deposition modelling of polylactic acid. *Progress in Additive Manufacturing, 8*(5), 775–799. https://doi.org/10.1007/s40964-022-00356-w

Sandanamsamy, L., Mogan, J., Rajan, K., Harun, W. S. W., Ishak, I., Romlay, F. R. M., et al. (2023). Effect of process parameter on tensile properties of FDM printed PLA. *Materials Today: Proceedings*. https://doi.org/10.1016/j.matpr.2023.03.217

Schmidt, A. M., & Kyosev, Y. (2023). Particle based simulation of the polymer penetration into porous structures during the fused deposition modelling. *Journal of Manufacturing Processes, 101*, 1205–1213. https://doi.org/10.1016/j.jmapro.2023.06.040

Shanmugam, V., Das, O., Babu, K., Marimuthu, U., Veerasimman, A., Johnson, D. J., et al. (2021). Fatigue behaviour of FDM-3D printed polymers, polymeric composites and architected cellular materials. *International Journal of Fatigue, 143*(106007), 1–15. https://doi.org/10.1016/j.ijfatigue.2020.106007

Singh, J., Kumar Goyal, K., & Kumar, R. (2022). Effect of filling percentage and raster style on tensile behavior of FDM produced PLA parts at different build orientation. *Materials Today: Proceedings, 63*, 433–439. https://doi.org/10.1016/j.matpr.2022.03.444

Song, Y., Ghafari, Y., Asefnejad, A., & Toghraie, D. (2024). An overview of selective laser sintering 3D printing technology for biomedical and sports device applications: Processes, materials, and applications. *Optics and Laser Technology*. https://doi.org/10.1016/j.optlastec.2023.110459

Tavangarian, F., Sadeghzade, S., Fani, N., Khezrimotlagh, D., & Davami, K. (2024). 3D-printed bioinspired spicules: strengthening and toughening via stereolithography. *Journal of the Mechanical Behavior of Biomedical Materials, 155*(106555), 1–12. https://doi.org/10.1016/j.jmbbm.2024.106555

Vakharia, V. S., Kuentz, L., Salem, A., Halbig, M. C., Salem, J. A., & Singh, M. (2021). Additive manufacturing and characterization of metal particulate reinforced polylactic acid (Pla) polymer composites. *Polymers, 13*(20), 1–16. https://doi.org/10.3390/polym13203545

Wang, X., Jiang, M., Zhou, Z., Gou, J., & Hui, D. (2017). 3D printing of polymer matrix composites: A review and prospective. *Composites Part b: Engineering, 110*, 442–458. https://doi.org/10.1016/j.compositesb.2016.11.034

Zohdi, N., Nguyen, P. Q. K., & Yang, R. (2024). Evaluation on material anisotropy of acrylonitrile butadiene styrene printed via fused deposition modelling. *Applied Sciences, 14*(5), 1–26. https://doi.org/10.3390/app14051870